Enhanced thermoelectric performance through tuning bonding energy in $Cu_2Se_{1-x}S_x$ liquid-like materials

Kunpeng Zhao,[†,‡] Anders Bank Blichfeld,[∥,↷] Hongyi Chen,[†,‡] Qingfeng Song,[†,‡] Tiansong Zhang,[†] Chenxi Zhu,[†,‡] Dudi Ren,[†] Riley Hanus,[⊥] Pengfei Qiu,[*,†] Bo B. Iversen,[∥] Fangfang Xu,[†] G. Jeffrey Snyder,[⊥] Xun Shi,[*,†] and Lidong Chen,[*,†,§]

[†]State Key Laboratory of High Performance Ceramics and Superfine Microstructure, Shanghai Institute of Ceramics, Chinese Academy of Sciences, Shanghai 200050, China.

[‡]University of Chinese Academy of Sciences, Beijing 100049, China.

[∥]Centre for Materials Crystallography, Department of Chemistry and iNANO, Aarhus University, Langelandsgade 140, DK-8000 Aarhus C, Denmark.

[↷]Department of Materials Science and Engineering, NTNU Norwegian University of Science and Technology, Trondheim NO-7491, Norway

[⊥]Department of Materials Science and Engineering, Northwestern University, Evanston, IL 60208, USA.

[§]Shanghai Institute of Materials Genome, Shanghai 200444, China.

ABSTRACT: Thermoelectric materials require an optimum carrier concentration to maximize electrical transport and thus thermoelectric performance. Element-doping and composition off-stoichiometry are the two general and effective approaches to optimize carrier concentrations, which have been successfully applied in almost all semiconductors. In this study, we propose a new strategy coined as bonding energy variation to tune the carrier concentrations in Cu_2Se-based liquid-like thermoelectric compounds. By utilizing the different bond features in Cu_2Se and Cu_2S, alloying S at the Se-sites successfully increases the bonding energy to fix Cu atoms in the crystal lattice to suppress the formation of Cu vacancies, leading to much lowered carrier concentrations toward the optimum value. Combing the lowered electrical and lattice thermal conductivities, and the relatively good carrier mobility caused by the weak alloy scattering potential, ultrahigh zTs are achieved in slightly S doped Cu_2Se with a maximum value of 2.0 at 1000 K, 30% higher than that in nominally-stoichiometric Cu_2Se.

1. Introduction

In the past twenty years, thermoelectric (TE) technology has attracted renewed interest due to the increasing concern on the global energy crisis and greenhouse gas emissions.[1-6] Using the Seebeck effect and Peltier effect, TE technology can realize a direct conversion between heat and electricity. Due to its advantages of no moving parts, no noise generation, and offering exceptional reliability, TE technology shows a great potential in applications such as power generation and electronic refrigeration.[7,8] The energy conversion efficiency of a TE material is evaluated by the dimensionless TE Figure of merit zT $=\alpha^2 T/\rho\kappa$, where α is the Seebeck coefficient, ρ is the electrical resistivity, T is the absolute temperature, and κ is the thermal conductivity. The quantity α^2/ρ is called the power factor (*PF*), which is associated with the electrical transport. Because the variations of α and $1/\rho$ are in a complete opposite direction when shifting carrier concentrations, there exists an optimal carrier concentration (p_{opt}) to maximize the *PF* and zT values.[9,10] For TE semiconductors, the carrier concentrations can vary nine orders of magnitude from 10^{13} to 10^{22} cm^{-3}.[11] However, the optimum carrier concentration in TE materials is usually limited

1

within one order of magnitude and the numerical values are dependent on the specific material system. Therefore, the carrier concentration in TE materials must be tuned to realize optimum values for high *PF* and *zT* values.

Element-doping and composition off-stoichiometry are the two general and effective approaches to tune carrier concentrations, which have been successfully applied in almost all TE semiconductors.[12-17] The former approach usually uses elements with different charge states to dope into the crystal lattice to alter the charge density of the material. However, the doping elements easily introduce carrier scattering centers to lower the carrier mobility or to change the electronic band structures, which might deteriorate the electrical transport. The latter one usually shifts the chemical compositions of TE semiconductors to alter the lattice defects and thus to change carrier concentrations.[18, 19] This method is limited by the thermodynamic equilibrium state of the material and thus it usually provides a small space to tune carrier concentrations since a large compositional variation is normally unacceptable in most semiconductors.[15] However, for some materials with a large intrinsic range of lattice defects such as many Cu- and Ag-based semiconductors, it is possible to tune carrier concentrations in a wide range through introducing composition off-stoichiometry to change the content of lattice defects.[20-23] However, this is also restricted by the thermodynamic state of the material that limit the space to tune carrier concentrations with the kind and concentration of carriers depending on specific material systems. For example, the variation ranges of hole concentrations are completely different in various Cu-based TE materials by using the normal sample fabrication processes, such as from $>10^{20}$ cm^{-3} to 1.0×10^{22} cm^{-3} for $Cu_{2-\delta}Se$,[24-27] 4.8×10^{18} cm^{-3} to 5.4×10^{21} cm^{-3} for $Cu_{2-\delta}S$,[23, 28] and 7×10^{20} cm^{-3} to at least 2.8×10^{21} cm^{-3} for $Cu_{2-\delta}Te$.[29, 30] Furthermore, dominant hole carriers are observed in almost all Cu-based compounds while dominant electron carriers are observed in many Ag-based compounds because of the feature of intrinsic lattice defects in these TE semiconductors.[21, 31, 32] Considering the same valence electron configuration of Cu/Ag and S/Se/Te, the discrepancy in the kind and concentration of carriers in these Cu- and Ag-based materials must come from the feature of chemical bonds that alter the lattice defects of the material. This implies that beyond the traditional element doping and composition off-stoichiometry, the carrier concentrations can also be tuned through varying chemical bonds. In this study, by introducing bonding energy variation through alloying S at the Se-sites in Cu_2Se (see **Figure 1**a), the carrier concentration is easily controlled down to 2.6×10^{20} cm^{-3}, close to its optimum value. Combining the much lowered lattice thermal conductivities, a maximum *zT* value about 2.0 at 1000 K is achieved, which is 30% higher than that in nominally-stoichiometric Cu_2Se (see Figure 1b).
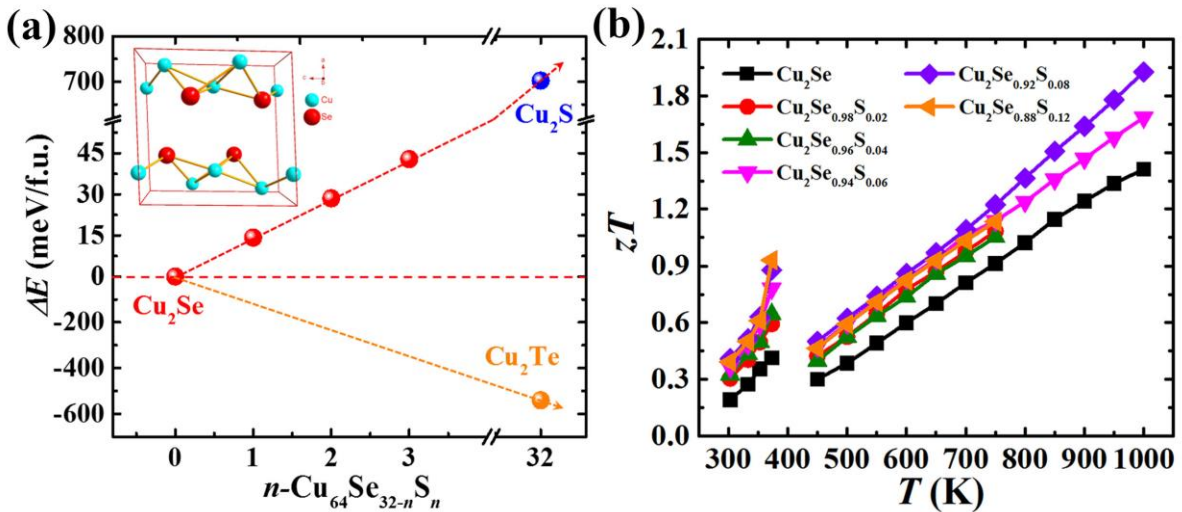

Figure 1. (a) Increased bonding energy (ΔE) as a function of S content in $Cu_{64}Se_{32-n}S_n$. The experimental lattice volume reduction is used for the calcualtions. The data of Cu_2S and Cu_2Te are also included for comparison. The crystal structure of Cu_2Se used for *ab initio* calculations are shown in the inset. (b) Temperature dependence of TE Figure of merit (*zT*) for $Cu_2Se_{1-x}S_x$ (*x*= 0, 0.02, 0.04, 0.06, 0.08 and 0.12).

2. Experimental and Calculation Section

2.1 Synthesis. Polycrystalline $Cu_2Se_{1-x}S_x$ (*x* = 0, 0.02, 0.04, 0.06, 0.08 and 0.12) were prepared by combining element-melting and longtime sample annealing processes. High purity raw elements, Cu (shot, 99.999%, Alfa Aesar), Se (shot, 99.999%, Alfa Aesar), and S (shots, 99.9999%, Alfa Aesar) were weighed out in stoichiometric proportions, loaded in pyrolitic boron nitride (P-BN) crucibles, and sealed in silica tubes under vacuum. The tubes were heated to 1423 K in 10 h and held at this temperature

for 12 h, and then cooled down to 923 K in 50 h. After annealing at 923 K for 8 days, the tubes were slowly cooled down to room temperature in 50 h. Some copper precipitates with red color on the surface were observed for Cu_2Se and the samples with low S content. The maximum mass of the copper precipitates weighs only about 0.4% of the total sample's weight, thus the initial nominal compositions are used for all $Cu_2Se_{1-x}S_x$ samples. After removing these copper precipitates, the annealed ingots were grounded into fine powders and sintered using the Spark Plasma Sintering (SPS, Sumitomo SPS-2040) equipment at around 753 K for 5 min under a pressure of 65 MPa. Electrically insulating and thermally conducting BN layers were sprayed onto the carbon foils and the inner sides of the graphite die before the sintering process in order to prohibit DC pulsed currents going through the powders. Several Cu-deficient $Cu_{2-y}Se$ (y = 0.02, 0.05, and 0.1) samples were also prepared using the same method for data comparison.

2.2 Characterization. Powder X-ray diffraction data were collected on a Rigaku, Rint 2000 with a Cu-Kα_1 source. The data were analyzed by Rietveld refinements performed in the *MAUD* program.[33] The main phase was modelled using the new low temperature structure from the recently published average structure of β-$Cu_{2-y}Se$ (ICSD-4321181)[34] with the Se to S ratio adjusted to reflect the nominal compositions. Secondary cubic (high temperature or high y) phase was observed for x = 0, 0.02, 0.04; α-$Cu_{2-y}Se$ with y = 0.25 (ICSD-150758). The cell parameters and the phase fraction were refined for each phase. The β-$Cu_2Se_{1-x}S_x$ phase was modeled using an anisotropic particle size as well as microstrain, with peak widths depending on the *hkl* values,[35] which arise from the intrinsic platelet particle shape, as seen from Figure 2. The particle shape was extended to $L_{max} = 4$, giving 4 refinable parameters for the particle size, and 4 parameters for microstrain in the $R\bar{3}m$ space group. For x = 0.06, 0.08 and 0.12 a March-Dollase model was used for (00*l*) reflections to model preferred orientation. Unit cell parameters, and the *x* and *y* atomic coordinates were refined and constrained so that Cu2 stayed on the mirror plane. All general Wyckoff sites had atomic coordinates refined. The ADPs (U_{iso}) were refined for all atoms, with Cu1a and Cu1b constrained to have equivalent ADPs. Furthermore, the occupancy for Cu1a and Cu1b was constrained to sum to unity. The results from the refinements of β-$Cu_2Se_{1-x}S_x$, including the copper deficient α-$Cu_{1.75}Se$ phase, are listed in Table S3 and the individual data and refinements plotted in Figure S3. The α-$Cu_{2-x}Se$ phase was refined using an isotropic particle size model. The diffraction peak at $2\theta = \sim 38.5°$ stems from the supercell, as described by Eikeland *et al.*[34] The sample morphologies were measured by field emission scanning electron microscopy (FESEM, Magellan-400) equipped with energy dispersive X-ray analysis (EDS, Horiba 250). The TEM examination was performed on a JEM-2100F field-emission transmission electron microscope. The samples for TEM were firstly ground into

fine powder, then ultrasonic dispersed in alcohol, finally deposited on the copper grid with carbon film. The photoelectron spectra (XPS) were measured on pressed pellets by using a Thermo Fisher Scientific ESCALAB 250 with monochromatic Al Kα X-ray (1486.74 eV). The carbon 1s peak was used as a reference to calibrate the binding energies of the other core level spectra. The speed of sound data were obtained by use of a Panametrics NDT 5800 pulser/receiver head; the response was recorded with a Tektronix TDS 1012 digital oscilloscope. The resistivity (ρ) and Seebeck coefficient (α) were measured simultaneously using an Ulvac ZEM-3 system. Thermal diffusivity (D) was measured using the laser flash method (Netzsch, LFA-457). Specific heat (C_p) was determined by differential scanning calorimetry (Netzsch DSC 404F3). The densities (d) were measured by the Archimedes method. The total thermal conductivity (κ) was calculated according to the relationship $\kappa = dC_pD$. Uncertainties in the electrical conductivity, Seebeck coefficient, and thermal diffusivity were ±4-9%, ±4%, and ±5-10%, respectively.[36] Hall coefficient (R_H) at 300 K was collected using a physical properties measurement system (PPMS-9, Quantum Design, USA). The hole concentration (p) was calculated by $p = 1/R_He$, where e was the elementary charge. Hall carrier mobility (μ_H) was calculated according to the relation $\mu_H = R_H/\rho$.

2.3 Density Functional Calculation. The bonding energy and Cu-ion vacancy formation energy of $Cu_2Se_{1-x}S_x$ were calculated using the Density-functional theory (DFT) implemented in the Vienna ab initio simulation package. The crystal structure of Cu_2Se is quite complicated and multiple structures may coexist at room temperature, as revealed by the TEM examination.[37] Until recently, an average structure of the compound was proposed by Eikeland *et al.*[34] However, all the Cu ions in this structure partially occupy their atomic sites, which can not be directly used for the first principle calculations. Thus here, we selected one of most similar room temperature crystal structures (space group P21/c) proposed by Nguyen et al. for the first principle calculations.[38] The basis Cu atoms occupy 2 different 4e Wyckoff positions: Cu1 (0.06444, -0.42110, 0.17094) and Cu2 (-0.19990, -0.07620, -0.00724). The basis Se atoms occupy a third 4e Wyckoff position: Se (0.29649, 0.06260, 0.34271). A series of 2 × 2 × 2 $Cu_{64}Se_{32-n}S_n$ super cells with different S-alloying content (n = 0, 1, 2, and 3) was constructed. Firstly, we performed the structural relaxation after adding S into Cu_2Se. However, the lattice volume reduction was too much after relaxation (see Table S1). For example, when adding one S into Cu_2Se, the volume of unit cell was reduced about 3.409%, which was one order of magnitude larger than the experimental data (0.363%, see Table S1 and Figure 2c). Thus we tried to use the experimental volume reduction to run the calculations. Besides, the data with no volume change were also included for comparison. All the data were shown in Table S1. Then, the difference of the cohesive energy between the S-included composition and the S-free $Cu_{64}Se_{32}$ com-

3

position was defined as the increased bonding energy ΔE by assuming that the change of the cohesive energy was dominated by the modification of the chemical bonds. For the compositions with $n = 2$ and 3, three different atomic configurations (see Table S2) were taken into account to calculate ΔE. The results for different atomic configurations were almost the same, and the average value was used in Figure 1. In addition, using the cohesive energy of Cu_2Se as a baseline, the increased bonding energy of Cu_2S and Cu_2Te with room temperature structures were also calculated for comparision. The Cu-ion vacancy formation energy $\Delta E_{(vacancy)}$ was calculated by the formula $\Delta E_{(vacancy,n)} = E_{(Cu_{63}Se_{32-n}S_n)} + E_{(Cu)} - E_{(Cu_{64}Se_{32-n}S_n)}$, where $E_{(Cu)}$ is the cohesive energy of copper with fcc crystal structure. The projector-augmented wave method (PAW) combined with the generalized gradient approximation of Perdew-Burke and Ernzerhof (PBE) was applied. To ensure sufficient accuracy, a cutoff energy of 400 eV, an energy convergence criterion of 10^{-5} eV and a regular Monkhorst-Pack k-point mesh of $5\times 5\times 5$ were applied.

3. Results and discussion

Cu_2X-based (X=S, Se, and Te) compounds are good liquid-like TE materials with ultralow lattice thermal conductivity (κ_L) and high zT.[23, 25, 29] The nature of Cu vacancies makes them display p-type conduction with holes as the dominant charge carriers. The chemical bond features in Cu_2X (X = S, Se or Te) are different, leading to the high hole concentrations in Cu_2Se (typically above 6.3×10^{20} cm^{-3}) and Cu_2Te (above 7×10^{20} cm^{-3}),[29, 39, 40] while much lower hole concentrations are observed in Cu_2S (down to 4.8×10^{18} cm^{-3}),[23] at least two orders of magnitude difference. The high hole concentration in Cu_2Se and Cu_2Te suggests high contents of Cu vacancies, and this implies the existence of weak chemical bonds. Otherwise, the Cu atoms should be captured in the lattice instead of the formation of Cu vacancies. In this simple model the low hole concentration in Cu_2S suggests that its chemical bonds are stronger than that in Cu_2Se. This is well confirmed by our *ab initio* calculations. As shown in Figure 1a, when introducing one S atom ($n = 1$) into a Se-site ($Cu_{64}Se_{31}S$), the total energy of the $2 \times 2 \times 2$ super cell (with 64 Cu atoms and 32 Se atoms in total) is improved with a value of 455.6 meV, i.e., 14.2 meV/f.u.. When keeping increasing the S content, the increased bonding energy ΔE is further increased to 28.5 meV/f.u. for $n=2$ and 42.8 meV/f.u. for $n=3$. In contrast, introducing Te atoms into Se-sites clearly reduces the bonding energy (see Figure 1a). The enhanced bonding energy in $Cu_2Se_{1-x}S_x$ is very beneficial to fix Cu atoms in the crystal lattice, resulting in much high Cu vacancy formation energy (shown in Figure S1) and correspondingly low concentration of Cu vacancies. Therefore, introducing S into Cu_2Se can signifi-

cantly improve its bond feature and thus lower hole concentrations, while introducing Te into Cu_2Se will lower the bonding energy and thus create more Cu vacancies resulting in high hole concentrations.

Figure 2a shows the room temperature powder X-ray diffraction (PXRD) patterns for $Cu_2Se_{1-x}S_x$ ($x=$ 0, 0.02, 0.04, 0.06, 0.08 and 0.12). The measurements were carried out on the powder samples that were ground from the annealed ingots after completely removing the copper precipitates on the surface. Most of the X-ray diffraction peaks are indexed to the Cu_2Se β-phase (trigonal, $R\bar{3}m$),[34] implying that Cu_2Se β-phase is the major phase in all solid solutions at room temperature. Besides, the diffraction peaks belonging to the Cu_2Se α-phase (cubic, $Fm\bar{3}m$) also appear in the XRD pattern of Cu_2Se, $Cu_2Se_{0.98}S_{0.02}$, and $Cu_2Se_{0.96}S_{0.04}$. According to the Cu-Se binary diagram,[24] at room temperature, Cu_2Se α-phase only appears when the Cu/S atomic ratio significantly deviates off the nominal chemical stoichiometry 2:1. Then, the observation of Cu_2Se α-phase at room temperature proves that the amount of Cu vacancies in our Cu_2Se sample should be very large, which is consistent with the visible severe copper precipitation phenomenon shown in Figure S2. Interestingly, using the same fabrication method, it seems that the copper precipitation is suppressed for the $Cu_2Se_{1-x}S_x$ solid solutions and the content of copper precipitates on the surface is reduced with increasing the S-alloying content. Taking $Cu_2Se_{0.94}S_{0.06}$ as an example, the surface of the ingot shown in Figure S2 is very clean. No obvious copper precipitates are observed after the annealing process. Correspondingly, the content of Cu vacancies in the S-alloyed samples should be also reduced, which can be well reflected by the amount of Cu_2Se α-phase detected from the XRD patterns. Figure 1b shows a selected range in the XRD patterns for the $Cu_2Se_{1-x}S_x$ solid solutions at 2θ = 42°-46°. Clearly, the intensity of the peak at 44.2°, which belongs to the Cu-deficient Cu_2Se α-phase, gradually decreases with increasing the S-alloying content. When the S-alloying content is around 0.06, the peak at 44.2° has almost completely disappeared, indicating that the Cu_2Se α-phase is not present and the content of Cu vacancies is reduced. In other words, the actual Cu content in the $Cu_2Se_{1-x}S_x$ solid solutions with higher S-alloying content would be much closer to the nominal chemical stoichiometry. This is consistent with our calculations that S improves bonding energy between Cu ions and anion-sublattice, which is beneficial for keeping Cu atoms inside the crystal structure. The lattice parameters were obtained from the Rietveld refinement based on the trigonal average structure of Cu2Se proposed by Eikeland *et al.*.[34] The lattice parameters linearly decrease with increasing S content, which is attributed to the small atomic size of S (1.04 Å) as compared with Se (1.17 Å).
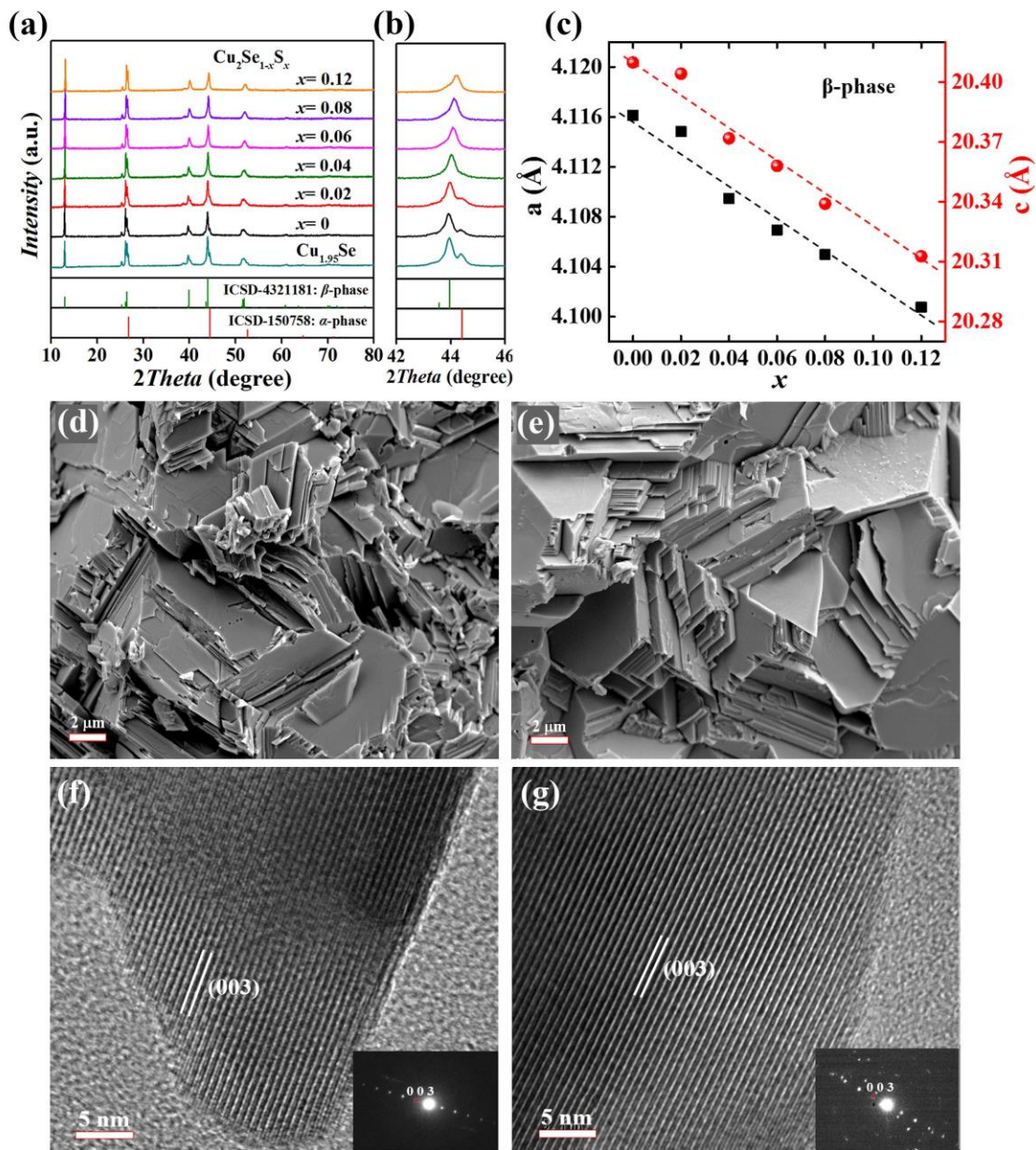
Figure 2. (a) Room temperature powder X-ray diffraction patterns for $Cu_2Se_{1-x}S_x$ (x= 0, 0.02, 0.04, 0.06, 0.08 and 0.12) ingots after annealing process. The data of $Cu_{1.95}Se$ are also included for comparison. The diffraction peak at 2θ = ~ 38.5° stems from the supercell, as described by Eikeland *et al.*[34] (b) Amplified X-ray diffraction patterns at 2θ = 42°-46°. (c) Lattice parameters calculated by structural Rietveld refinement based on the average structure of Cu_2Se proposed by Eikeland *et al.*[34] Fractured secondary electron (SE) images for the sintered sample Cu_2Se (d) and $Cu_2Se_{0.88}S_{0.12}$ (e). High resolution TEM images for the sintered sample (f) Cu_2Se and (g) $Cu_2Se_{0.88}S_{0.12}$.

The elemental energy-dispersive X-ray spectroscopy mappings carried out on the bulk materials after sintering process indicate that all elements are homogeneously distributed in the matrix without any secondary phases (see Figure S4). Combing all the data strongly suggests that all S atoms enter into the crystal lattice of Cu_2Se. Figure 2d-e shows the microstructure examined by FESEM on the cross-sections of sintered Cu_2Se and $Cu_2Se_{0.88}S_{0.12}$ products. The typical microstructure of a sandwich-like stacking of thin plates with the thickness <100 nm is clearly observed, consistent with the layered crystal structure shown in the inset of Figure 1a. High resolution TEM images shown in Figure 2f-g confirm that these layers are oriented along the (003) crystal face.
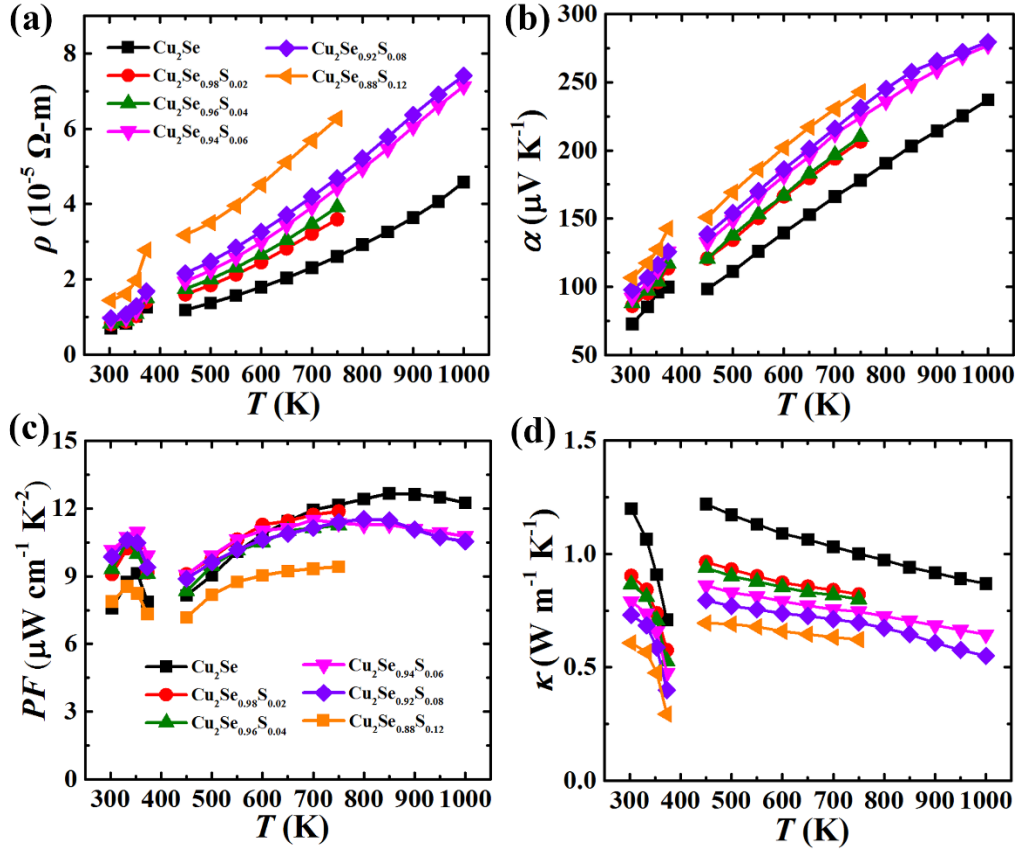
Figure 3. Temperature dependences of (a) resistivity ρ, (b) Seebeck coefficient α, (c) power factor PF and (d) total thermal conductivity κ for $Cu_2Se_{1-x}S_x$ (x= 0, 0.02, 0.04, 0.06, 0.08 and 0.12).

The thermoelectric properties of $Cu_2Se_{1-x}S_x$ (x= 0, 0.02, 0.04, 0.06, 0.08 and 0.12) are shown in Figure 3 that cover both low-temperature trigonal phase and high-temperature cubic phase. The data near 400 K induced by the phase transition from the trigonal phase to the cubic phase are not shown. In addition, some samples show abnormal low thermal diffusivity above 750 K (see Figure S5), thus their TE properties are also not shown here. The electrical resistivity (ρ) of Cu_2Se increases with increasing temperature, displaying a typical metallic-like behavior. The presence of Cu vacancies leads to p-type electrical transport with positive Seebeck coefficients in Cu_2Se. Although the S-alloyed Cu_2Se samples still display similar metallic-like electrical transport behavior, both the resistivity and Seebeck coefficient are obviously increased with increasing the S content throughout the whole measured temperature range. Besides, the electrical properties are well maintained to at least 850 K, which is 100 K higher than the sintering temperature. This indicates that our samples should reach the equilibration state after the sintering process. Based on the measured ρ and α, the power factors ($PF = \alpha^2/\rho$) of $Cu_2Se_{1-x}S_x$ are calculated and shown in Figure 3c. The PFs of $Cu_2Se_{1-x}S_x$ are almost the same as for Cu_2Se except for $Cu_2Se_{0.88}S_{0.12}$, which has a slightly decreased value. Figure 3d shows the total ther-

mal conductivity κ as a function of temperature. Clearly, the κ values are much lowered when alloying S into Cu_2Se although the samples possess similar PFs. When keeping increasing S content, κ gradually decreases in the entire temperature range. At 450 K, the κ for $Cu_2Se_{0.88}S_{0.12}$ is 0.7 W m^{-1} K^{-1}, only about half of that for Cu_2Se.

The significantly enhanced electrical resistivity and Seebeck coefficient are attributed to the successful reduction of hole concentrations (p) by alloying S, which is shown in **Figure 4**a. In Cu_2Se we find a high hole concentration of 5.3×10^{20} cm^{-3} due to the presence of Cu vacancies. When introducing S into Cu_2Se, the hole concentration is notably decreased. In particularly, the room temperature p is reduced to about 2.6×10^{20} cm^{-3} in $Cu_2Se_{0.88}S_{0.12}$, only a half of that in Cu_2Se although S has the same valence electron configuration as Se. The X-ray photoelectron spectroscopy measurements (see Figure S7) indicate that the valence states of Cu and Se in $Cu_2Se_{1-x}S_x$ is +1 and -2, respectively, the same as those in Cu_2Se. Therefore, the decreased hole concentrations in $Cu_2Se_{1-x}S_x$ must come from the reduction of the content of Cu vacancies although the actual density of Cu vacancies is difficult to measure experimentally. This is consistent with our calculations shown above. Because S-alloying strengthens the chemical bonds, the Cu atoms tend to be

6

captured in the crystal lattice instead of moving out from the crystal lattice.

In order to better understand the electrical transport properties, a single parabolic band (SPB) model is used.[41, 42] Based on the Fermi statistics, the Seebeck coefficient α can be expressed as

$$\alpha = \frac{k_B}{e}\left[\frac{(2+\lambda)F_{\lambda+1}(\eta)}{(1+\lambda)F_\lambda(\eta)} - \eta\right] \qquad ,(1)$$

where k_B is the Boltzmann constant, e is the electron charge, λ is the scattering factor with a value of 0 for a mixed carrier scattering combining acoustic phonon and alloy scattering based on our mobility data (shown in Figure S8), and η ($=E_F/k_BT$) is the reduced Fermi energy. The Fermi integrals are given by $F_m(\eta) = \int_0^\infty \frac{x^m dx}{1+\exp(x-\eta)}$, where x is the reduced carrier energy. The Hall carrier concentration can also be expressed as a function of Fermi integrals

$$p = 4\pi\left(\frac{2m^*k_BT}{h^2}\right)^{3/2}\frac{F_{1/2}(\eta)}{r_H} \qquad ,(2)$$

$$r_H = \frac{3}{4}\frac{F_{1/2}(\eta)F_{-1/2}(\eta)}{F_0{}^2(\eta)} \qquad ,(3)$$

where m^* is the electronic effective mass and r_H is the Hall factor. The calculated Pisarenko plot (α vs. p) at 300 K is shown in Figure 4b by using the SPB model with a m^* of 2.3 m_e, where m_e is the free electron mass. Clearly, the experimental α data of $Cu_2Se_{1-x}S_x$ follow the calculated line. In addition, as shown in Figure 4b, the data of the Cu-deficient $Cu_{2-y}Se$ samples (y = 0.02, 0.05, and 0.1) also agree well with the calculated line. This strongly suggests that S-alloying just shifts the Fermi level upward without significantly affecting the electronic band structures of Cu_2Se near the Fermi level. Considering that Cu_2Se is a degenerate semiconductor with a large band gap (about 1.2 eV), we assume that the carrier concentrations are virtually unchanged from room temperature to high temperatures. Then the Pisarenko plots (α vs. p) at 750 K are also plotted in Figure 4b with a m^* of 3.2 m_e. Just as for the 300 K data, all the $Cu_2Se_{1-x}S_x$ samples display a similar trend as the Cu-deficient $Cu_{2-y}Se$ samples (y = 0.02, 0.05, and 0.1), suggesting that the discussion mentioned above also works at high temperatures.

We also investigated the carrier mobilities (μ_H) when introducing S into Cu_2Se because μ_H is another key factor to affect electrical transport. Around room temperature, acoustic phonon scattering is the dominating carrier scattering mechanism for the Cu-deficient $Cu_{2-y}Se$ samples (y = 0, 0.05, and 0.1) (see Figure S8), This is supported by the scenario shown in Figure 4c where the carrier mobilities follow the green dashed line calculated based on the acoustic phonon scattering. For $Cu_2Se_{1-x}S_x$, the introduced S atoms in the Cu_2Se lattice lead to a mixed carrier scattering mechanism including acoustic phonon and alloying scattering. Therefore, the carrier mobilities in $Cu_2Se_{1-x}S_x$ obviously deviate from the green dashed line (see Figure 4c). We thus re-calculated the carrier mobilities by covering both acoustic phonon and alloying scatterings (see the violet solid line) and these calculations agree well with the experimental data. The calculation details are shown in the Supporting Information with a deformation potential Ξ of 4.3 eV and an alloy scattering potential U of 0.24 eV for $Cu_2Se_{1-x}S_x$. Interestingly, the latter one is rather small as compared with the typical U values observed in most semiconductors with the values of about 0.6-2 eV.[43] Even compared with the value of 1.1 eV in Br-doped Cu_2Se by Day et al.,[13] the U value in our samples is much lower. The low U value means the less deterioration of the carrier mobilities. This is consistent with the experimental data shown in Figure 4c in which the carrier mobilities for $Cu_2Se_{1-x}S_x$ are much higher than those for Br-doped Cu_2Se samples. The same valence states and relative small electronegativity difference between S and Se are believed to be responsible for the weak potential energy fluctuation and consequently weak deterioration on carrier mobility observed in the present study.
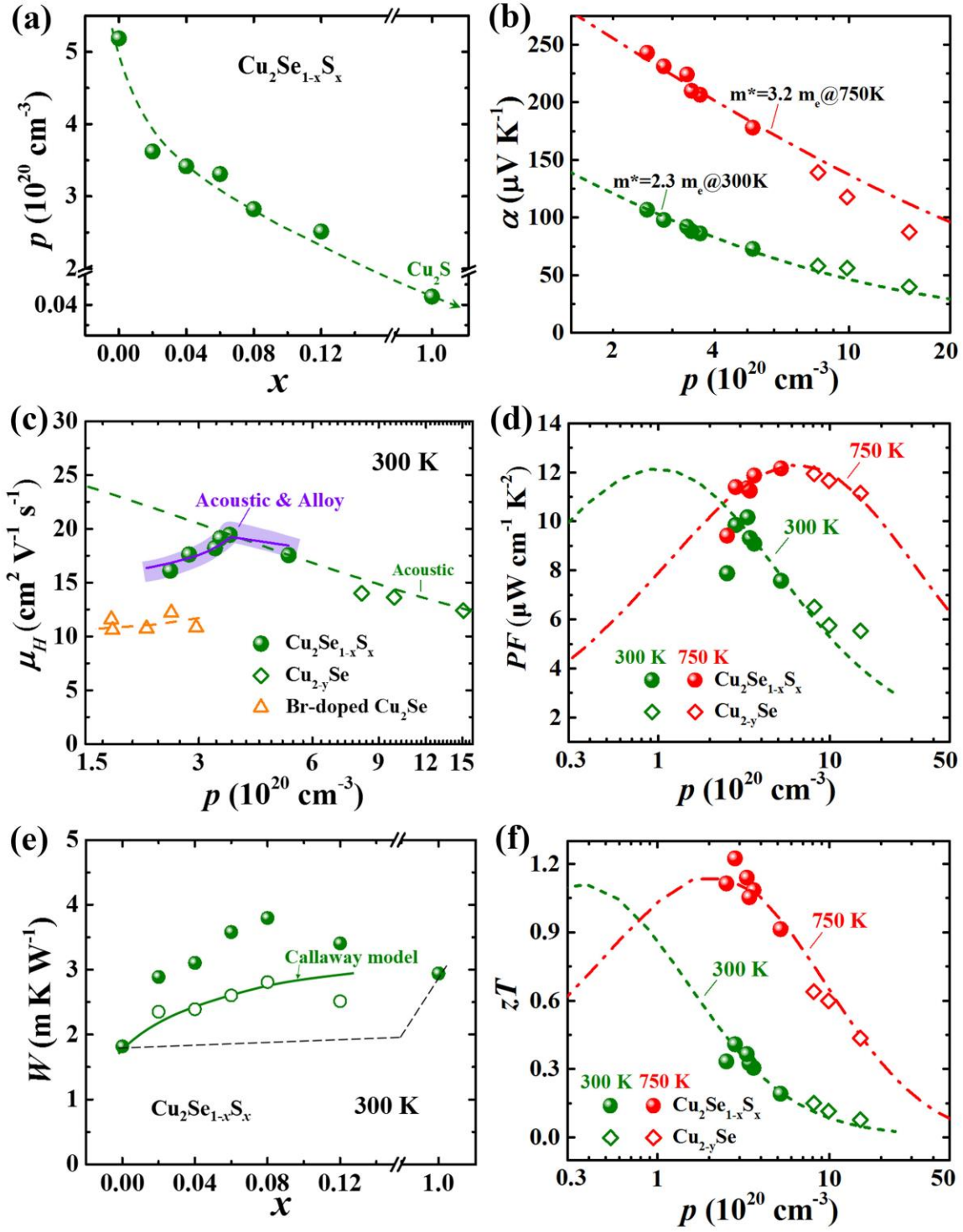
Figure 4. (a) Hall carrier concentration (p) as a function of S content for $Cu_2Se_{1-x}S_x$ (x= 0, 0.02, 0.04, 0.06, 0.08 and 0.12). (b) Experimental and calculated Pisarenko plots (α *vs.* p) at 300 K and 750 K. The lines are the calculated curves based on the single parabolic band (SPB) model. (c) Hall mobility (μ_H) *vs.* Hall carrier concentration at 300 K. The green dashed line is calculated assuming that the acoustic phonon scattering is the dominant one. The violet solid line is calculated assuming a combined acoustic phonon and alloy scatterings. The data of Cu-deficient $Cu_{2-y}Se$ samples (open symbols) and Br-doped Cu_2Se samples are also included for comparison. (d) Power factor (*PF*) *vs.* Hall carrier concentration at 300 K and 750 K. The dashed lines are calculated based on the SPB model. (e) Lattice thermal resistivity (*W*) as a function of S content at 300 K. The filled circles are experimental *W* data, and the open ones are the data after the deduction of reduced sound velocity in $Cu_2Se_{1-x}S_x$. The dashed black line represents the variation according to the mixing rule, and the

8

solid green line is the calculated curve by the Callaway model.[49, 50] (f) zT vs. Hall carrier concentration at 300 K and 750 K. The dashed lines are calculated based on the SPB model. The data of Cu-deficient $Cu_{2-y}Se$ samples (open symbols) are also included for comparison.

According to Equation 1-3 and Equation S1-S4 in the Supporting Information, the power factor ($PF = pe\mu_H\alpha^2$) at 300 K and 750 K as a function of carrier concentration (room temperature data) is calculated and plotted in Figure 4d. The experimental data agree well with the calculated curves at both 300 K and 750 K. The maximum PFs occur at the carrier concentration of around 1×10^{20} cm^{-3} at 300 K and 6×10^{20} cm^{-3} at 750 K. Due to the existence of natural Cu vacancies, the hole concentration in $Cu_{2-y}Se$ can be lowered to 4.8×10^{20} cm^{-3}, which is far larger than the optimum hole concentrations for high power factors at 300 K (see Figure 4d). However, when altering bonding energy through alloying S at Se sites, the hole concentrations are lowered with the values toward the optimum values at 300 K and completely covering the optimum values at 750 K (Figure 4d). This is also consistent with the experimental results shown in Figure 3c with the improved power factors at 300 K, and maintained or only slightly lowered power factors at 750 K for the $Cu_2Se_{1-x}S_x$. As discussed below, the lowered hole concentrations are also very beneficial for suppressing the carrier thermal conductivity and thus achieving high zTs.

The thermal conductivity is lowered through alloying S at Se sites. The total κ includes two parts, termed the lattice thermal conductivity (κ_L) and the carrier thermal conductivity (κ_c). The former is contributed by the lattice vibrations, while the latter one directly proportional to the carrier concentration and mobility. Here, the carrier thermal conductivity (κ_c) is evaluated by the Wiedemann-Franz law ($\kappa_c = L_0T/\rho$, where L is the Lorenz number with a value of 1.5×10^{-8} V^2 K^{-2} for Cu_2Se-based materials[44]) and plotted in Figure S9a. Because the introduced S atoms in Cu_2Se suppress the formation of Cu vacancies and thus decrease the carrier concentrations, a much decreased κ_c is observed with the reduction values almost proportional to the hole concentration (see Figure S9a-b). Figure S10 also presents the lattice thermal conductivities (κ_L) for $Cu_2Se_{1-x}S_x$ by subtracting κ_c from the total κ. Very low κ_L values are observed for all the samples. The sudden reduction in κ_L around 380-400 K is attributed to the phase transitions.[24, 45] The weak κ_L temperature dependence above 400 K is the key character of CuX-based TE compounds, which has been also observed in almost all other liquid-like TE materials.[46-48] Alloying S leads to quickly and gradually decreased κ_L values in the entire temperature range (see Figure S10).

The lattice thermal conductivity are directly related with the heat capacity (C_V), speed of sound (v), and phonon mean free path (l). Thus we firstly measured the speed of sound for all samples and the results are shown in Figure S11. The longitudinal speed of sound v_l in Cu_2Se_{1-} $_xS_x$ solid solutions are almost the same as in Cu_2Se. However, the transverse speed of sound v_t are lower than those in Cu_2Se and Cu_2S. The abnormally low transverse speed of sound in $Cu_2Se_{1-x}S_x$ are similar to those in Cu_2S, in which an unusually low transverse speed of sound is observed with a normal large longitudinal speed of sound as compared with Cu_2Se. But this is different from the normal mixing rule of two matrix compounds in which the speed of sound should be between the two matrix compounds. We guess that adding S into Cu2Se can lead to more complicated unit cell because one new type of atoms is added into the structure. This can also lead to the extra local strains because the atomic sizes between S and Se are much different. All these can significantly affect the phonon dispersions and speed of sound. In order to know the details, the phonon calculations are required for future study. Because the speed of sound are much reduced in $Cu_2Se_{1-x}S_x$, we firstly calculate this part of contribution based on the equation of $\kappa_L = 1/3C_Vvl$ and then get the changed lattice thermal resistivity (open circles in Figure 4e) Next, we use the Callaway model to calculate the contributions from mass and strain fluctuation phonon scatterings.[49, 50] The calculation details are shown in the Supporting Information. The mass fluctuation scattering parameter Γ_M and the strain field fluctuation scattering parameter Γ_S, as a function of S alloying content, are shown in Figure S12. It is clear that the strain fluctuations contribute more to the reduction of lattice thermal conductivity than mass fluctuations in $Cu_2Se_{1-x}S_x$.

Based on the measured α, ρ and κ, the dimensionless TE Figure of merit zT ($=\alpha^2T/\rho\kappa$) is calculated and shown in Figure 1b. Introducing bonding differentiation by alloying S at the Se sites greatly improved zTs in the entire temperature range due to the lowered hole concentrations toward to the optimum value, suppressed carrier and lattice thermal conductivity, and well maintained high PFs. A maximum zT value of 2.0 is achieved at 1000 K for $Cu_2Se_{0.92}S_{0.08}$, which is 30% higher than that for Cu_2Se. We also calculated the zT curves based on Equation 1-3 and Equation S1-S4 in the Supporting Information under the assumption that κ_L is the same (0.5 W m^{-1} K^{-1}) for all samples. The results are shown in Figure 4f. All the data, for both $Cu_2Se_{1-x}S_x$ and $Cu_{2-y}Se$, show a very nice agreement with the calculated curves. The optimum hole concentration for the maximized zT is usually slightly lower than that for power factor because of the contribution from electronic thermal conductivity. In this study, although the hole concentrations in $Cu_2Se_{1-x}S_x$ at 750 K are slightly lower than the optimum value for power factors, they fall well in the range corresponding to the peak zTs (see Figure 4f). This is also strongly supported by the

9

temperature dependence of *zTs* shown in Figure 1b, in which the *zT* values of $Cu_2Se_{1-x}S_x$ are much higher than that of Cu_2Se in the whole temperature range. Interestingly, our study shows that the *zTs* can be much enhanced at 300 K if the hole concentrations could be further reduced to the order of 10^{19} cm^{-3} (see Figure 4f), which should stir interests for low temperature studies and applications of Cu_2Se-based materials in the future.

The temperature gradient and current density are very small during TE property measurements. During the measurements, the thermoelectric properties can be reproducible after thermal cycles.[23, 25, 51] Furthermore, the contribution from Cu ions to the total electrical properties in these good liquid-like TE materials is less than 3%.[52] Therefore, the contribution from Soret-like effects is expected small (<3%). The service stability is significantly deteriorated under large temperature gradient and/or large currents in these liquid-like materials. However, the recent study shows that their stability can be improved.[53] This is the key concern for the liquid-like TE materials. If the problem of stability is solved, these liquid-like materials are expected to have great potentials for real applications.

4. Conclusions

To sum up, we demonstrate a successful example to enhance the TE performance in Cu_2Se liquid-like materials by using the bonding energy variation approach. Through slight alloying of S at the Se-sites, the crystal structure of Cu_2Se is well maintained but the bonding energy is significantly increased. This much-improved bonding energy helps to fix the Cu atoms within the crystal lattice instead of formation of Cu vacancies. Thus the hole concentrations are significantly reduced down to 2.6×10^{20} cm^{-3}, close to the optimum value predicated by the SPB model. In addition, relatively high carrier mobilities are observed due to the weak alloy scattering potential. Finally, alloying S into Cu_2Se also decrease both the electrical and the lattice thermal conductivities due to the lowered hole concentrations and reduced transverse speed of sound. Combing all these effects, the *zTs* in slightly S doped Cu_2Se are significantly improved with a maximum value of 2.0 at 1000 K, 30% higher than that in nominally-stoichiometric Cu_2Se. We expect that this method is effective to optimize carrier concentrations in semiconducting materials with an initial large range of lattice defects caused by the composition off-stoichiometry. Many Cu- and Ag-based compounds are typical examples of such behavior as we particularly show in this study for the Cu_2X-based materials.

ASSOCIATED CONTENT

Supporting Information. Calculation details for carrier mobility and Callaway model; results for energy calculations, Table S1; different atomic configurations for energy calculations, Table S2; Refined parameters and quality factors Table S3; Cu vacancy formation energy, Figures S1; copper precipitates, Figure S2; Rietveld refinement patterns, Figure S3; EDS result, Figures S4; thermal diffusivity,Figure S5; specific heat and HT-XRD patterns Figures S6; XPS core level spectra, Figures S7; carrier concentration and carrier mobility, Figures S8; carrier thermal conductivity, Figures S9; lattice thermal conductivity, Figures S10; speed of sound, Figures S11; scattering parameters, Figure S12; repeatability test on electronic transport properties, Figure S13; thermogravimetric curve, Figure S14. This material is available free of charge via the Internet at http://pubs.acs.org.

AUTHOR INFORMATION

Corresponding Author

* E-mail for S.X.: xshi@mail.sic.ac.cn
* E-mail for C.L.: cld@mail.sic.ac.cn
* E-mail for P.Q.*:* qiupf@mail.sic.ac.cn

Notes

The authors declare no competing financial interest.

REFERENCES

(1) Li, Z.; Xiao, C.; Zhu, H.; Xie, Y. Defect Chemistry for Thermoelectric Materials. *J. Am. Chem. Soc.* **2016**, *138*, 14810-14819.
(2) Yang, J.; Yip, H. L.; Jen, A. K. Y. Rational Design of Advanced Thermoelectric Materials. *Adv. Energy Mater.* **2013**, *3*, 549-565.
(3) Shi, X.; Chen, L.; Uher, C. Recent advances in high-performance bulk thermoelectric materials. *Int. Mater. Rev.* **2016**, *61*, 379-415.
(4) Tan, G.; Zhao, L. D.; Kanatzidis, M. G. Rationally Designing High-Performance Bulk Thermoelectric Materials. *Chem. Rev.* **2016**, *116*, 12123-12149.
(5) Zeier, W. G.; Zevalkink, A.; Gibbs, Z. M.; Hautier, G.; Kanatzidis, M. G.; Snyder, G. J. Thinking like a Chemist: Intuition in Thermoelectric Materials. *Angew. Chem. Int. Edit.* **2016**, *55*, 6826-6841.
(6) Yang, J.; Xi, L.; Qiu, W.; Wu, L.; Shi, X.; Chen, L.; Yang, J.; Zhang, W.; Uher, C.; Singh, D. J. On the tuning of electrical and thermal transport in thermoelectrics: an integrated theory–experiment perspective. *npj Comput. Mater.* **2016**, *2*, 15015.

(7) Zhang, Q. H.; Huang, X. Y.; Bai, S. Q.; Shi, X.; Uher, C.; Chen, L. D. Thermoelectric Devices for Power Generation: Recent Progress and Future Challenges *Adv. Eng. Mater.* **2016,** *18,* 194-213.

(8) Shi, X.; Chen, L. Thermoelectric materials step up. *Nat. Mater.* **2016,** *15,* 691-692.

(9) Snyder, G. J.; Toberer, E. S. Complex thermoelectric materials. *Nat. Mater.* **2008,** *7,* 105-114.

(10) Pei, Y. Z.; Gibbs, Z. M.; Gloskovskii, A.; Balke, B.; Zeier, W. G.; Snyder, G. J. Optimum Carrier Concentration in n-Type PbTe Thermoelectrics. *Adv. Energy Mater.* **2014,** *4,* 1400486.

(11) Madelung, O., *Semiconductors: data handbook*. Springer Science & Business Media: 2012.

(12) Hao, F.; Qiu, P.; Tang, Y.; Bai, S.; Xing, T.; Chu, H. S.; Zhang, Q.; Lu, P.; Zhang, T.; Ren, D.; Chen, J.; Shi, X.; Chen, L. High efficiency Bi2Te3-based materials and devices for thermoelectric power generation between 100 and 300 °C. *Energy Environ. Sci.* **2016,** *9,* 3120-3127.

(13) Day, T. W.; Weldert, K. S.; Zeier, W. G.; Chen, B.-R.; Moffitt, S. L.; Weis, U.; Jochum, K. P.; Panthöfer, M.; Bedzyk, M. J.; Snyder, G. J. Influence of Compensating Defect Formation on the Doping Efficiency and Thermoelectric Properties of Cu$_{2-y}$Se$_{1-x}$Br$_x$. *Chem. Mater.* **2015,** *27,* 7018-7027.

(14) Zhang, Q.; Chere, E. K.; Sun, J.; Cao, F.; Dahal, K.; Chen, S.; Chen, G.; Ren, Z. Studies on Thermoelectric Properties of n-type Polycrystalline SnSe$_{1-x}$S$_x$ by Iodine Doping. *Adv. Energy Mater.* **2015,** *5,* 1500360.

(15) Wang, X.; Qiu, P.; Zhang, T.; Ren, D.; Wu, L.; Shi, X.; Yang, J.; Chen, L. Compound defects and thermoelectric properties in ternary CuAgSe-based materials. *J. Mater. Chem. A* **2015,** *3,* 13662-13670.

(16) Han, C. G.; Zhang, B. P.; Ge, Z. H.; Zhang, L. J.; Liu, Y. C. Thermoelectric properties of p-type semiconductors copper chromium disulfide CuCrS$_{2+x}$. *J. Mater. Sci.* **2013,** *48,* 4081-4087.

(17) Wang, S.; Yang, J.; Wu, L.; Wei, P.; Yang, J.; Zhang, W.; Grin, Y. Anisotropic Multicenter Bonding and High Thermoelectric Performance in Electron-Poor CdSb. *Chem. Mater.* **2015,** *27,* 1071-1081.

(18) Pomrehn, G. S.; Zevalkink, A.; Zeier, W. G.; van de Walle, A.; Snyder, G. J. Defect-Controlled Electronic Properties in AZn2Sb2 Zintl Phases. *Angew. Chem. Int. Ed.* **2014,** *126,* 3490-3494.

(19) Zhao, L.; Wang, X.; Fei, F. Y.; Wang, J.; Cheng, Z.; Dou, S.; Wang, J.; Snyder, G. J. High thermoelectric and mechanical performance in highly dense Cu$_{2-x}$S bulks prepared by a melt-solidification technique. *J. Mater. Chem. A* **2015,** *3,* 9432-9437.

(20) Wei, T. R.; Li, F.; Li, J. F. Enhanced Thermoelectric Performance of Nonstoichiometric Compounds Cu$_{3-x}$SbSe$_4$ by Cu Deficiencies. *J. Electron. Mater.* **2014,** *43,* 2229-2238.

(21) Mi, W.; Qiu, P.; Zhang, T.; Lv, Y.; Shi, X.; Chen, L. Thermoelectric transport of Se-rich Ag2Se in normal phases and phase transitions. *Appl. Phys. Lett.* **2014,** *104,* 133903.

(22) Yang, L.; Chen, Z.-G.; Han, G.; Hong, M.; Zou, J. Impacts of Cu deficiency on the thermoelectric properties of Cu$_{2-x}$Se nanoplates. *Acta Mater.* **2016,** *113,* 140-146.

(23) He, Y.; Day, T.; Zhang, T.; Liu, H.; Shi, X.; Chen, L.; Snyder, G. J. High Thermoelectric Performance in Non-Toxic Earth-Abundant Copper Sulfide. *Adv. Mater.* **2014,** *26,* 3974-3978.

(24) Kang, S. D.; Danilkin, S. A.; Aydemir, U.; Avdeev, M.; Studer, A.; Snyder, G. J. Apparent critical phenomena in the superionic phase transition of Cu$_{2-x}$Se. *New J. Phys.* **2016,** *18,* 013024.

(25) Liu, H.; Shi, X.; Xu, F.; Zhang, L.; Zhang, W.; Chen, L.; Li, Q.; Uher, C.; Day, T.; Snyder, G. J. Copper ion liquid-like thermoelectrics. *Nat. Mater.* **2012,** *11,* 422-425.

(26) Ohtani, T.; Tachibana, Y.; Ogura, J.; Miyake, T.; Okada, Y.; Yokota, Y. Physical properties and phase transitions of β Cu$_{2-x}$Se (0.20≤ x≤ 0.25). *J. Alloys Compd.* **1998,** *279,* 136-141.

(27) Su, X.; Fu, F.; Yan, Y.; Zheng, G.; Liang, T.; Zhang, Q.; Cheng, X.; Yang, D.; Chi, H.; Tang, X.; Zhang, Q.; Uher, C. Self-propagating high-temperature synthesis for compound thermoelectrics and new criterion for combustion processing. *Nat. Commun.* **2014,** *5,* 4908.

(28) Qiu, P.; Zhu, Y.; Qin, Y.; Shi, X.; Chen, L. Electrical and thermal transports of binary copper sulfides Cu$_x$S with x from 1.8 to 1.96. *APL Mater.* **2016,** *4,* 104805.

(29) He, Y.; Zhang, T.; Shi, X.; Wei, S.-H.; Chen, L. High thermoelectric performance in copper telluride. *NPG Asia Mater.* **2015,** *7,* 210.

(30) Ballikaya, S.; Chi, H.; Salvador, J. R.; Uher, C. Thermoelectric properties of Ag-doped Cu2Se and Cu2Te. *J. Mater. Chem. A* **2013,** *1,* 12478.

(31) Qiu, P.; Shi, X.; Chen, L. Cu-based thermoelectric materials. *Energy Storage Mater.* **2016,** *3,* 85-97.

(32) Guin, S. N.; Srihari, V.; Biswas, K. Promising thermoelectric performance in n-type AgBiSe2: effect of aliovalent anion doping. *J. Mater. Chem. A,* **2015,** *3,* 648-655.

(33) Lutterotti, L. Total pattern fitting for the combined size–strain–stress–texture determination in thin film diffraction. *Nucl. Inst. Methods Phys. Res. B* **2010,** *268,* 334-340.

(34) Eikeland, E.; Blichfeld, A. B.; Borup, K.A.; Zhao, K.; Overgaard, J.; Shi, X.; Chen, L.; Iversen, B.B. Crystal structure across the β to α phase transition in thermoelectric Cu$_{2-x}$Se. *IUCr-J* **2017,** https://doi.org/10.1107/S2052252517005553.

(35) Popa, N. The (hkl) dependence of diffraction-line broadening caused by strain and size for all Laue groups in Rietveld refinement. *J. Appl. Crystallogr.* **1998,** *31,* 176.

(36) Wang, H.; Porter, W.; Böttner, H.; König, J.; Chen, L.; Bai, S.; Tritt, T.; Mayolett, A.; Senawiratne, J.; Smith, C.; Harris, F.; Sharp, J.; Lo, J.; Kleinke, H.; Kiss, L. Annex VIII–Thermoelectric Materials for Waste Heat Recovery: An International Collaboration for Transportation Applications. *ORNL/TM* **2011,** 434.

[37] Lu, P.; Liu, H.; Yuan, X.; Xu, F.; Shi, X.; Zhao, K.; Qiu, W.; Zhang, W.; Chen, L. Multiformity and fluctuation of Cu ordering in Cu$_2$Se thermoelectric materials. *J. Mater. Chem. A* **2015,** *3,* 6901

(38) Nguyen, M. C.; Choi, J. H.; Zhao, X.; Wang, C. Z.; Zhang, Z.; Ho, K. M. New Layered Structures of Cuprous Chalcogenides as Thin Film Solar Cell Materials: Cu2Te and Cu2Se. *Phys. Rev. Lett.* **2013,** *111,* 165502.

(39) Gahtori, B.; Bathula, S.; Tyagi, K.; Jayasimhadri, M.; Srivastava, A. K.; Singh, S.; Budhani, R. C.; Dhar, A. Giant enhancement in thermoelectric performance of copper selenide by incorporation of different nanoscale dimensional defect features. *Nano Energy* **2015,** *13,* 36-46.

(40) Wu, L.; Su, X.; Yan, Y.; Uher, C.; Tang, X. Ultra-Fast One-Step Fabrication of Cu2Se Thermoelectric Legs With Ni–Al Electrodes by Plasma-Activated Reactive Sintering Technique. *Adv. Eng. Mater.* **2016,** *18,* 1181.

(41) Goldsmid, H. J., *Introduction to thermoelectricity*. Springer: 2010.

(42) May, A. F.; Toberer, E. S.; Saramat, A.; Snyder, G. J. Characterization and analysis of thermoelectric transport in n-type Ba$_8$Ga$_{16-x}$Ge$_{30+x}$. *Phys. Rev. B* **2009,** *80,* 125205.

(43) Wang, H.; LaLonde, A. D.; Pei, Y.; Snyder, G. J. The Criteria for Beneficial Disorder in Thermoelectric Solid Solutions. *Adv. Funct. Mater.* **2013,** *23,* 1586-1596.

(44) Zhao, L. L.; Wang, X. L.; Wang, J. Y.; Cheng, Z. X.; Dou, S. X.; Wang, J.; Liu, L. Q. Superior intrinsic thermoelectric perfor-

mance with zT of 1.8 in single-crystal and melt-quenched highly dense $Cu_{(2-x)}Se$ bulks. *Sci. Rep.* **2015**, *5*, 7671.

(45) Liu, H.; Yuan, X.; Lu, P.; Shi, X.; Xu, F.; He, Y.; Tang, Y.; Bai, S.; Zhang, W.; Chen, L.; Lin, Y.; Shi, L.; Lin, H.; Gao, X.; Zhang, X.; Chi, H.; Uher, C. Ultrahigh Thermoelectric Performance by Electron and Phonon Critical Scattering in Cu2Se1-xIx. *Adv. Mater.* **2013**, *25*, 6607-6612.

(46) Pei, Y.; Heinz, N. A.; Snyder, G. J. Alloying to increase the band gap for improving thermoelectric properties of Ag2Te. *J. Mater. Chem.* **2011**, *21*, 18256.

(47) Weldert, K. S.; Zeier, W. G.; Day, T. W.; Panthofer, M.; Snyder, G. J.; Tremel, W. Thermoelectric transport in Cu_7PSe_6 with high copper ionic mobility. *J. Am. Chem. Soc.* **2014**, *136*, 12035-40.

(48) Bhattacharya, S.; Basu, R.; Bhatt, R.; Pitale, S.; Singh, A.; Aswal, D. K.; Gupta, S. K.; Navaneethan, M.; Hayakawa, Y. Cu-CrSe2: a high performance phonon glass and electron crystal thermoelectric material. *J. Mater. Chem. A* **2013**, *1*, 11289.

(49) Callaway, J.; Baeyer, H. C. Effect of point imperfections on lattice thermal conductivity. *Phys. Rev.* **1960**, *120*, 1149.

(50) Meisner, G.; Morelli, D.; Hu, S.; Yang, J.; Uher, C. Structure and lattice thermal conductivity of fractionally filled skutterudites: Solid solutions of fully filled and unfilled end members. *Phys. Rev. Lett.* **1998**, *80*, 3551.

(51) Zhao, K.; Qiu, P.; Song, Q.; Blichfeld, A.; Eikeland, E.; Ren, D.; Ge, B.; Iversen, B.; Shi, X.; Chen, L.; Ultrahigh thermoelectric performance in $Cu_{2-y}Se_{0.5}S_{0.5}$ liquid-like materials, *Mater. Tod. Phy. X* (**2017**) accepted.

(52) Balapanov M.; Nadejzdina A.; Yakshibayev; Lukmanov D.; Gabitova R. Ionic conductivity and chemical diffusion in $Li_xCu_{2-x}Se$ superionic alloys. *Ionics*, **1999**, 5, 20-22.

(53) Kang S.; Pohls J.; Aydemir U.; Qiu P.; Stoumpos C.; Hanus R.; White M; X. Shi, Chen L.; M.G. Kanatzidis, G.J. Snyder, Enhanced stability and thermoelectric figure-of-merit in copper selenide by lithium doping, *Mater. Tod. Phy. X* (**2017**) accepted.

The table of contents entry: Beyond element-doping and composition off-stoichiometry, we propose a new strategy coined as bonding energy variation to tune the carrier concentrations in Cu_2Se-based liquid-like thermoelectric compounds, leading to a maximum zT value of 2.0 at 1000 K, 30% higher than that in nominally-stoichiometric Cu_2Se.